In-situ study of keyhole behavior during a laser pulse applied to the dissimilar metal joint

Iryna Tomashchuk, Mélanie Duband, Jean-Marie Jouvard

Metall. Res. Technol. **120**, 412 (2023)

https://doi.org/10.1051/metal/2023043

Metallurgical Research & Technology

Available online at:
www.metallurgical-research.org

Original Article Open Access

In-situ study of keyhole behavior during a laser pulse applied to the dissimilar metal joint★

Iryna Tomashchuk*, Mélanie Duband, and Jean-Marie Jouvard

Laboratoire Interdisciplinaire Carnot de Bourgogne, UMR CNRS-6303, Université de Bourgogne, 12 rue de la Fonderie, 71200 Le Creusot, France

Received: 18 October 2022 / Accepted: 15 April 2023

Abstract. In the present study, the method of frontal observation of the keyhole through the fused quartz window is applied to the dissimilar combinations between stainless steel 316L and different metals chosen to illustrate four typical cases of mismatch in physical properties: a much lower vaporization temperature (316L/magnesium alloy AZ31), a much higher vaporization temperature (316L/pure niobium), a more reflective and conductive metal (316L/aluminum alloy A5754) and an extremely reflective metal (316L/pure copper). A standalone Yb:YAG laser pulse was applied to the dissimilar couple/quartz and metal/quartz joints. Each of these cases was studied using image treatment of the obtained high-speed videos and post-mortem observation of the interaction zone. Basing on the analysis of the physical properties of the metals and their interdependencies, the first criterion of keyhole development in the dissimilar joint is proposed. It is concluded that in case of Yb:YAG laser welding of stainless steel with metals having thermal conductivity $\leq$200 $W \cdot m^{-1} \cdot K^{-1}$, the keyhole development is dominant in the metal having lower vaporization temperature, while for the 316L combinations with the metals having thermal conductivity >200 $W \cdot m^{-1} \cdot K^{-1}$, the keyhole development remains dominant on the 316L side, but its progression is slowed down by the neighboring metal.

Keywords: laser welding / dissimilar joining / high-speed imaging / keyhole

1 Introduction

Since the first studies on dissimilar welding of metals, it was noticed that the material combinations having an important mismatch in physical properties, such as fusion and vaporization temperatures, form quite asymmetrical melted zones that can become problematic in view of controlling the melted zone composition. The dynamics of keyhole behavior in deep-penetration laser welding is decisive for the development of the melted zone as well as for the final joint quality. However, only few experimental studies were dedicated to the investigation of the keyhole behavior during laser welding of dissimilar metals. Some dispersed evidences of a possible keyhole asymmetry were progressively accumulating in the available literature. The simplest evidence of the keyhole asymmetry in dissimilar laser welding is the shift of the melted zone root towards one of the metals, visible on the weld cross-section. For example, the titanium/tantalum combination [1] demonstrated the shift of a melted zone root from the joint line towards the metal with a lower vaporization temperature (titanium), which reflects the respective offset of the keyhole. The combination of the metallographic observation of the weld cross-section with high-speed imaging of the melt surface allowed proving the pronounced keyhole asymmetry during the laser welding of Ti-6Al-4V/niobium couple [2]: the keyhole was shifted towards Ti-6Al-4V that has a lower vaporization temperature. The same tendency was observed during the high-speed imaging of a pulsed laser welding between aluminum and magnesium alloys [3]: the keyhole was strongly shifted on the magnesium alloy that has a lower vaporization temperature. On the other hand, in case of laser joining of a highly reflective metal such as copper with a less reflective metal, the melted zone is strongly shifted away from the reflective metal. Such observations were made for the partially penetrated copper/steel [4] and copper/nickel [5] welds. Moreover, the root of the melted zone in both cases was also shifted away from copper, which must reflect the respective shift of the keyhole. Based on the above, it can be concluded that the mismatches in vaporization temperatures and in absorption coefficients of laser radiation are two key factors of a keyhole asymmetry. However, nowadays the systematic study of these factors remains limited to the numerical simulation proposed in [6]. In this study,

★ Special Issue on 'Laser Applications for Metallic Materials Processing', edited by Sophie Costil and Matthieu Schneider.

* e-mail: iryna.tomashchuk@u-bourgogne.fr

the asymmetry of the keyhole due to the mismatch in vaporization temperatures between the reference metal (titanium or copper) and a random associated metal was quantified by two parameters measurable on the cross-section of the joint: a relative keyhole area and a relative offset of the keyhole root from the joint line. The linear increase of the keyhole area in a reference material with the rise of vaporization temperature of a random associated material was observed, but it appeared to be much lower in case of a highly reflective reference material such as copper. The position of the keyhole root was strongly determined by the absorptivity of the reference material: in case of copper, it was usually shifted towards the opposite material, and returned on the joint line only in case of its very high vaporization temperature of the neighbor metal. On the contrary, in case of a well-absorbing reference metal such as titanium, the keyhole root always remained on titanium side and shifted away from the joint line with the increase of the vaporization temperature of the opposite material.

In situ observation of the keyhole behavior would allow to quantify the existing asymmetry and get a better understanding of the role of the abovementioned influencing factors on the keyhole development, as well as validate the existing numerical models and their conclusions. The post-mortem microscopic evaluation of keyhole shape is difficult due to the frequent collapse of its walls occurring before the end of solidification. The efficient capture of keyhole shape after the solidification of the melted zone can be achieved only for particular alloys such as Cu-Hf [7]. The high-speed imaging of the melt surface from above only shows the front of the keyhole [8] and allows measuring the top and bottom apertures [9], while the advanced techniques such as in-situ X-ray imagery [10] and optical coherence tomography [11] remain hardly accessible. The observation of the keyhole and the melted zone dynamics with use of the visually transparent ceramic material represents an interesting alternative. This relatively cheap and easy method allows the detailed observation of the insides of the keyhole. Jin et al. [12] used a standalone Pyrex-like borosilicate glass GG17 glass plate for the high-speed imaging of the lateral keyhole profile formed during continuous welding with a CO_2 laser. Later, Jin et al. [13] applied this material and same kind of laser for a simultaneous frontal and lateral observation of the keyhole using two high-speed cameras. The association of such visually transparent ceramics with a metal sheet or foil allowed observing the dynamics of the keyhole in metallic material. Zhang et al. [14] placed an aluminum film between two GG17 glass plates for high-speed imaging and spectroscopic measurements of the insides the keyhole created with a CO_2 laser. However, in this case the GG17 glass plate also absorbed CO_2 laser radiation and thus participated in keyhole dynamics. According to Zhang et al. [15], the laser radiation having $\lambda \sim 1\,\mu m$ produced by Nd:YAG, Yb:YAG, fiber and disk lasers, unlike the radiation of CO_2 laser, is not absorbed by borosilicate glass. Consequently, for these lasers, it is possible to induce the keyhole dynamics in the metal alone, while the glass melts only via heat conduction from the melted zone.

Zhang et al. [16] formulated the demands to a translucid material for the keyhole observation in the following way: (1) very low thermal expansion coefficient, (2) sharp gas-liquid and liquid-solid interfaces and important difference between the fusion and vaporization temperatures; (3) equal permeability to light emission for different wavelengths; (4) high ionization energy compared to the metal (which is useful for spectroscopic studies). The most accessible translucid material, soda-lime glass, is not suitable for this type of observations due to its high thermal expansion coefficient ($6.7 \times 10^{-7}\,K^{-1}$). Arata et al. [17] attempted to use soda lime glass for keyhole observation but obtained a low quality image due to the small difference between melting and vaporization temperatures. In many studies, a borosilicate glass GG17 ($T_{softening} = 1350\,K$, $T_{vap} = 1769\,K$, thermal expansion coefficient $3.3 \times 10^{-6}\ K^{-1}$) was used as a transparent material for the observation of the keyhole during the continuous laser welding. Zhang et al. [16] and then Jin et al. [18] observed the keyhole dynamics in aluminum foils placed between two GG17 glass plates and irradiated with CO_2 laser. Then, Chen et al. [19] used the similar configuration for the study of keyhole drilling during the standalone laser pulse on a thin molybdenum sheet, using Nd:YAG laser. Li et al. [20] used another configuration, where the fiber laser beam was equally shared between the bulk steel sheet and GG17 glass plate, which allowed approaching the plane symmetry condition of the keyhole observation. Then, Jiang et al. [21] used this approach for studying the effect of a reduced ambient pressure on the keyhole dynamics in steel, using Nd:YAG laser.

Fused quartz is another interesting material that satisfies the criterions of successful keyhole observation: it has even higher phase change temperatures ($T_{softening} = 1830\,K$ and $T_{vap} = 2503\,K$) and much lower thermal expansion coefficient ($5.5 \times 10^{-7}\ K^{-1}$) compared to GG17. Both materials have similar transmissivity (>95%) in $\sim 1\,\mu m$ spectral range. Due to the unique properties of fused quartz, the quartz/metal interface can be considered as a plane of symmetry [22]. Matteï et al. [23] successfully performed a frontal high-speed imaging of the keyhole in pure tin through the fused quartz plate during both pulsed and continuous laser welding. Then, Tomashchuk et al. [3] used the fused quartz for the observation of the keyhole development in dissimilar metal combination of aluminum/magnesium alloys having relatively low vaporization temperatures. However, as shows the study of Artinov et al., 2018 [22], the quartz plate was also able to resist in such extreme conditions as 18 kW Nd:YAG laser welding in combination with a 15 mm thick stainless steel.

The dissimilar welding of stainless steels to other metals is one of the most researched upon, but also the one of the most difficult, because of a profuse formation of brittle intermetallic phases with a big part of existing metals and alloys. The competitive keyhole development in the dissimilar butt joint should be understood and taken into account for a better process control. In the present study, the method of frontal observation of the keyhole through the fused quartz window is applied to the dissimilar metal/quartz combinations between stainless steel 316L and different metals chosen to illustrate four typical cases of

Table 1. Some physical properties of the used materials.

Materials properties	316L	AZ31	Nb	A5754	Cu	Fused quartz
$a_{\text{Yb:YAG}}$ at 300K[a]	0.28	0.08	0.13	0.06	0.04	<0.05
k at 300 K ($\text{W}\cdot\text{m}^{-1}\cdot\text{K}^{-1}$)	16.3	156	53.7	237	401	1.46
T_{melting} (K)	1648–1723	878–903	2750	883–902	1357	1830[b]
$T_{\text{vaporization}}$ (K)	3013	1363	5017	2792	2835	2503
L_{vap} ($\text{kJ}\cdot\text{mol}^{-1}$)	340	127	697	294	300	283

[a] Estimated for flat polished surfaces using equation (7).
[b] Softening temperature.

mismatch in physical properties: a much lower vaporization temperature (316L/magnesium alloy AZ31), a much higher vaporization temperature (316L/pure niobium), a more reflective and conductive metal (316L/aluminum alloy A5754) and an extremely reflective metal (316L/pure copper). The aim of the present study is to characterize the keyhole behavior in each of these cases using the image treatment of the obtained high-speed videos and post-mortem observations of the interaction zone, in order to extend the actual understanding of the keyhole asymmetry.

2 Experimental

The 3 mm thick rectified plates of 316L stainless steel, AZ31 magnesium alloy (3.5 wt.% Al, 1.4 wt.% Zn, 0.2 wt.% Mn, 0.1 wt.% Si, 0.05 wt.% Cu), A5754 aluminum alloy (3.6 wt.% Mg, 0.5 wt.% Mn, 0.4 wt.% Fe, 0.4 wt.% Si, 0.3 wt.% Cr, 0.2 wt.% Zn, 0.15 wt.% Ti, 0. 1 wt.% Cu), pure niobium, pure copper and fused quartz were used as base materials. The chosen physical properties of these materials are given in Table 1. The observation of the keyhole through the fused quartz window (Fig. 1) was performed according to [3]. A Yb:YAG laser Trumph 6001 with a spot diameter of 600 µm, a focal distance of 200 mm, a beam power of 3.5 kW and a pulse time of 6 ms was used. These operational conditions were chosen in order to obtain the keyholes that are deep enough (several mm) to allow the detailed observation using high-speed imagining. In order to visualize the keyhole progression on the dissimilar metal joint, the laser spot was centered on the intersection point between two metal plates and fused quartz plate, in order to have 50% of spot area on the optically transparent fused quartz and 25% of spot area on each metal. In all experiments, the beam axis was inclined to the left by 3° on the metal/quartz plane to avoid the eventual harmful reflection of the beam inside the optics. The plates were carefully clamped to avoid the gaps. No gas protection was used.

A high-speed imaging of keyhole formation was made from a frontal position using a high-speed camera Phantom V9.1 with 6400 fps, diaphragm 11, exposure time 15 µs and resolution 480 × 480 px. No additional illumination sources were used. The continuous thermal emission from the keyhole was observed through the 810 ± 3 nm bandpass filter. The dimensions of the observation area were fixed to 6.5 mm × 6.5 mm. Fiji software [24] was used for image processing, namely, an Otsu automatic threshold was used to define the profile of the keyhole. The observable area of the keyhole (*KH area* given in mm^2) and its penetration

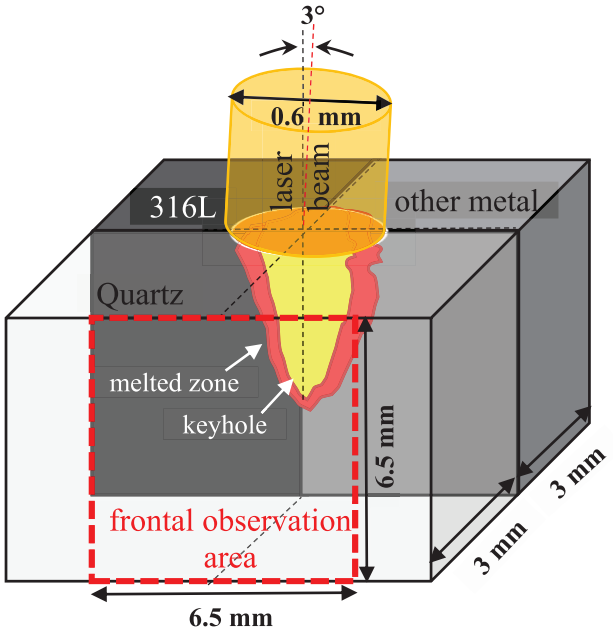

Fig. 1. The experimental configuration used for the observation of the dissimilar joint keyhole through the fused quartz window.

(H_{KH} given in µm) were measured for each image. In this manner, the keyhole development was observed for the triple combinations of quartz with AZ31/316L, niobium/316L, A5754/316L and copper/316L joints. Additionally, the visualization of the keyhole was performed for the binary metal/quartz combinations, by centering the laser beam on the metal/quartz plane. The imaging of these binary combinations was performed on the same plates that triple dissimilar combinations, in order to avoid the false conclusions induced by an eventual difference in clamping efficiency between the fused quartz and the metal plates. The dynamics of keyhole progression was represented by plotting the extracted keyhole depths (H_{KH}) in function of pulse time. For most cases, the first 1.5 ms of the keyhole formation were represented by a rapid nonlinear increase of the penetration that was followed by a slower linear progression. The slope of this linear part was considered as an average drilling rate of the keyhole in the following discussion.

In order to evaluate the influence of the fused quartz plate on the keyhole dimensions, 5 experiments were made with the 316L/316L joints according to the DODO method

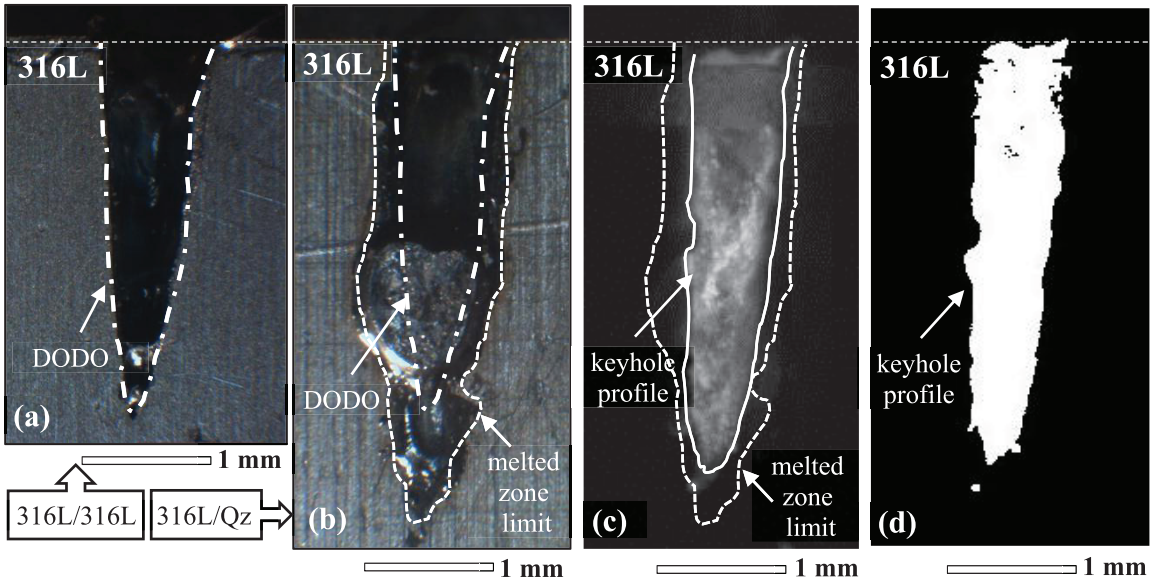

Fig. 2. The optical image of the melted zone of the 316L/316L (a) and the 316L/quartz (b) combinations; the keyhole shape as seen in the end of 6 ms pulse observed through a 810±3 nm band-pass filter (c) and after the application of Otsu automatic threshold (d).

proposed by Schneider et al. [25] and the obtained dimensions of the interaction zones were compared to those of 5 316L/quartz joints. The confidence interval associated to the impact dimensions was evaluated using a bilateral Student's *t*-distribution ($\alpha = 0.05$).

After the experiment, the metal/quartz joints were separated from the fused quartz plates and observed by optical microscopy and SEM JSM-6610LA (Jeol) equipped with EDS analyzer.

3 Results and discussion

3.1 The comparison between the 316L/316L and the 316L/quartz combinations

The difference between steel/steel and steel/quartz melted zones can be induced by the simultaneous effect of two following factors. On the one hand, the direct contact of steel with the less conductive fused quartz plate would promote the local accumulation of heat and the resulting expansion of the melted zone. On the other hand, the quasi-transparence of the fused quartz to Yb:YAG laser radiation should lead to the loss of ~50% of the total beam power (a half of the laser spot situated on the quartz side) and also make the multiple reflections inside the keyhole existing on the metal side less efficient. The comparison between 316L/316L and the 316L/quartz impacts (Figs. 2a and 2b) witnessed the domination of the first factor: the melted zone becomes 20% deeper ($3052 \pm 30\,\mu m \rightarrow 3683 \pm 43\,\mu m$) and 16% larger ($869 \pm 25\,\mu m \rightarrow 1008 \pm 77\,\mu m$) in presence of fused quartz plate. These results are in agreement with the observations reported by Guo et al. [26], who found higher penetrations of the laser-induced drilling at steel/GG17 glass interfaces compared to steel/steel combination, with conservation of global dynamics of drilling.

As the softening temperature of fused quartz is lower than that the vaporization temperature of the 316L (Tab. 1), the contact with keyhole walls induced the softening on the quartz side, and the limits of the melted zone became irregular (Fig. 2b). As the chosen operational conditions are close to the drilling regime, the loss of matter was systematically observed on the metal side of the impact, with formation of a 0.1–0.3 mm deep imprint of the keyhole. However, no pronounced depression was observed on the quartz side. The quartz plate remained crack-free and allowed observing in detail the insides of the bright keyhole (Fig. 2c) during the whole pulse duration, while the surrounded melted zone and unmelted material appeared dark. The similar observations were made for other tested metallic materials. The angle of 3° applied between the welding head and the verticality induced slight asymmetry of the interaction zone (Fig. 2), as the focal point was situated on the top surface of the joint.

The image treatment of the keyhole shape resulted in a regular enough profile (Fig. 2d) that was further used for the estimation of the quantitative characteristics. The final depths of the keyhole in the 316L/quartz joints observed on the different plates by the end of the pulse were comprised in the interval of $2965 \pm 365\,\mu m$. This incertitude is due to the variation of the laser beam centering on the metal/quartz interface and the varying time lapse between the last frame with laser "on" and the actual end of the pulse. The curves of observable keyhole areas in 316L/quartz combination obtained on different plates (far from the bimetallic joint) were rather concordant (Fig. 3), and an average area by the end of the pulse was evaluated to $1.62 \pm 0.47\ mm^2$. These results were found encouraging and were followed by the study of the binary metal/quartz and the triple 316L/metal/quartz combinations.

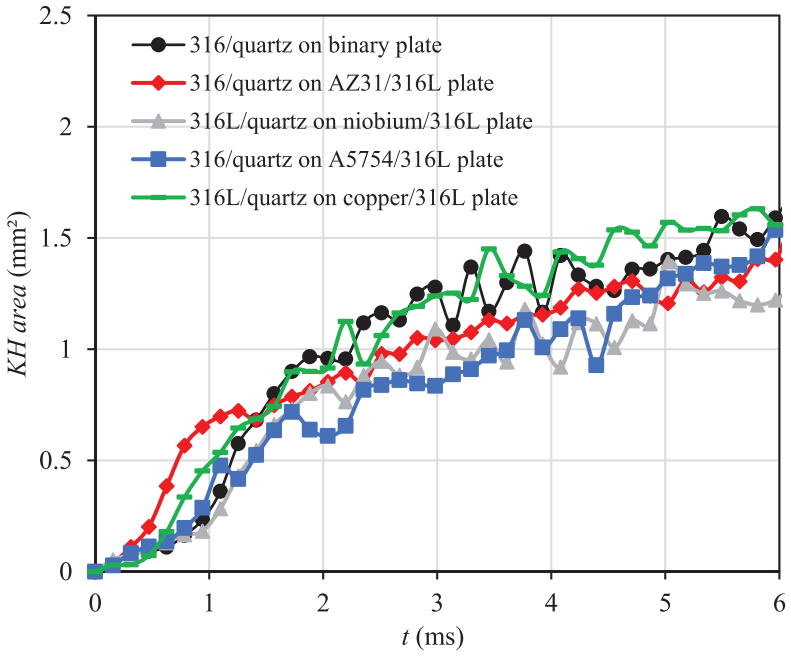

Fig. 3. The evolution of visible keyhole areas in 316L observed on different metal/quartz plates.

3.2 The observation of other binary metal/quartz combinations

Other binary metal/quartz combinations gave very different results, depending on the physical properties of the metal. However, in all cases, the fused quartz plates remained crack-free. The AZ31/quartz combination (Fig. 4a) resulted in a deep (5057 μm) and narrow (985 μm) melted zone due to a low vaporization temperature of magnesium alloy AZ31 (Tab. 1). The niobium/quartz combination (Fig. 4b) revealed only a 1107 μm deep and 1086 μm large melted zone. Such small melted zone is due to a very high vaporization temperature of niobium (Tab. 1).

The A5754/quartz combination formed an even smaller melted zone (Fig. 4c) with a depth of 746 μm and a width of 975 μm, because of a high thermal conductivity and a low absorption coefficient of the AA5754 alloy (Tab. 1). The copper/quartz combination did not result in the formation of the melted zone because of the very high thermal conductivity and a low absorption coefficient of copper.

The high-speed videos of the keyhole progression were treated with the same algorithm as for the 316L/quartz combination (Sect. 3.1). The extracted keyhole depths (H_{KH}) were used for calculation of drilling rates as described in the Experimental part (Sect. 2). The evolution of the observable keyhole areas is provided in Figure 5. These keyhole characteristics obtained for triple and binary metal/quartz combinations are compared and discussed in the following paragraphs.

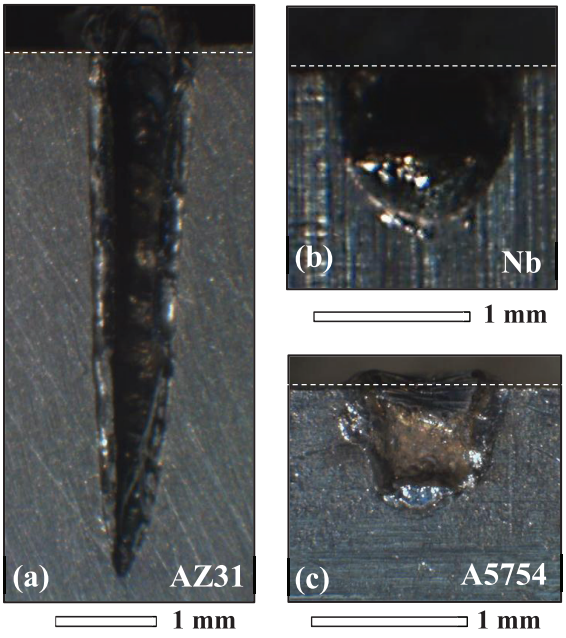

Fig. 4. The optical image of the melted zone of the AZ31/quartz (a), niobium/quartz (b) and A5754/quartz (c) impacts obtained in identical conditions.

3.3 The AZ31/316L dissimilar couple

The post-mortem observation of the impact zone at AZ31/316L interface after removing the quartz plate (Figs. 6a and 6b) showed the presence of the drilled cavity strongly shifted on AZ31 side that has much lower vaporization temperature. The X-mapping of the impact zone revealed the important adherences of the melted quartz and very limited mixing between the two metallic materials. The size of the melted zone was close to that observed for the binary AZ31/quartz combination (5066 μm in depth and 1300 μm in width). The root of the melted zone and the keyhole was shifted on AZ31 alloy by 122 μm (to the left).

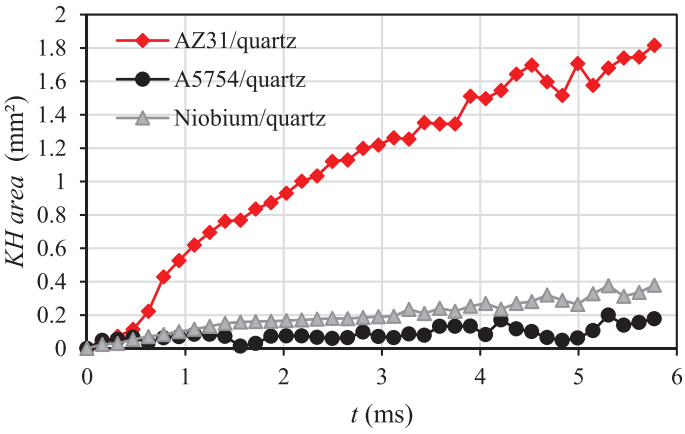

Fig. 5. The evolution of visible keyhole areas in different binary metal/quartz combinations.

The high-speed imaging (Fig. 6c) clearly showed the preferential development of the keyhole in the AZ31 alloy, while 316L side was involved only in the top part of the keyhole. From the very beginning of the pulse, both materials were involved in keyhole formation, however, the keyhole area on AZ31 side was growing continuously up to 1.55 mm^2 (which corresponds to 80% of total observable keyhole area), whereas on 316L side it quickly stabilized around 0.50 mm^2, as the bottom part of the keyhole became tangent to the joint line (Fig. 7a). The final observable keyhole area (2.05 mm^2) was very close to 1.82 mm^2 measured for binary AZ31/quartz joint (Fig. 5).

The keyhole depth evolution during the pulse (Fig. 7b) also witnessed the keyhole development controlled by the drilling on the AZ31 side: the AZ31 and AZ31/316L curves look almost identical, while the 316L curve shows a much slower increase. As expected, the drilling rate for the AZ31/316L couple (0.63 m/s) estimated for $t > 1.5$ ms was found very close to that of AZ31 (0.65 m/s), while the 316L showed an almost twice lower value (0.32 m/s).

These observations allow concluding that the pronounced asymmetry of the keyhole and the control of the drilling rate by the AZ31 side are determined by the preferential evaporation of magnesium alloy that has a 1650 K lower vaporization temperature compared to the 316L. The difference in absorption coefficients of these metallic materials does not seem to influence the behavior of the keyhole.

3.4 The niobium/316L dissimilar couple

Unlike the AZ31, niobium has a 2004 K higher vaporization temperature than the 316L. The produced melted zone was shared between the two materials and almost symmetrical (Figs. 8a and 8b). Unlike AZ31/316L, no pronounced cavity was visible post-mortem. The melted zone presented a strong mix between the components and contained important adherences of the melted quartz. The dimensions of the melted zone (2792 μm in depth and 1188 μm in width) were close to those of the 316L/quartz combination (Sect. 3.1). The keyhole was also shared between the two materials (Fig. 8c), with its root centered on the joint line. It was expected that the niobium side would be less involved in the keyhole formation; however, apparently, the used energy density was sufficient for attaining its vaporization temperature.

Due to its high vaporization temperature and thermal conductivity, niobium becomes significantly involved in the keyhole drilling starting from pulse duration >1 ms (Fig. 9a). The keyhole area on niobium side increases very slowly to reach 0.62 mm^2 (or 40% of the observable keyhole area), while it progresses rapidly on 316L side up to 1.07 mm^2. The final keyhole area (1.69 mm^2) is very close to that measured in 316L/quartz (1.62 ± 0.47 mm^2), while the keyhole area in niobium/quartz (0.38 mm^2) is much smaller (Fig. 5).

In the same way, at the start of the pulse, the depth of the keyhole at the dissimilar interface progressed very slowly and followed the curve of niobium (Fig. 9b). After $t = 1$ ms, it approached the curve of the 316L/quartz, however, the final depth was a little lower. It can be thus concluded that in the niobium/316L joint, the drilling of the keyhole is mainly controlled by the 316L side, however, it is slightly slowed down due to the important vaporization energy and higher thermal conductivity of niobium. The average drilling rates estimated for times >1.5 ms had equal values for the 316L/quartz and niobium/316L/quartz combinations (0.38 m/s), when the niobium/quartz couple had an almost 3 times lower drilling rate (0.12 m/s).

3.5 The A5754/316L dissimilar couple

An aluminum alloy A5754 formed with 316L a melted zone that was more developed on the A5754 side (Figs. 10a and 10b). It contained an important mix between the components and numerous quartz adherences. The dimensions of the melted zone (2721 μm in depth and 1848 μm in width) were much bigger than for the A5754/quartz couple and close to those of the 316L/quartz (Sect. 3.3). The preferential melting on the A5754 side was promoted by the contact of the aluminum alloy with the stainless steel having a much lower thermal conductivity, as well as by comparatively lower melting point of the A5754. On the other hand, the keyhole was more developed on the 316L side than on the A5754 side, and the root of the keyhole was shifted on the 316L side (to the right) by 170 μm (Fig. 10c). Such asymmetry can be attributed to the lower absorptivity of the laser radiation by the A5754 side as well as by its higher thermal conductivity.

The observable keyhole areas in 316L and A5754 were increasing in a similar manner during the pulse, and the final contribution of AA5754 represented 40% (Fig. 11a). The final keyhole area (1.04 mm^2) was intermediate between 1.62 ± 0.47 mm^2 measured in 316L/quartz (Sect. 3.1) and 0.18 mm^2 measured in A5754/quartz (Fig. 5). The contact with 316L (that has lower thermal conductivity along with higher vaporization temperature and absorptivity) promoted the involvement of AA5754 in keyhole formation. The depth of the keyhole in the A5754/316L joint was following the curve of the 316L/quartz, but progressively deviated towards the lower values for $t >$ 1.5 ms, which can be attributed to the contribution of a

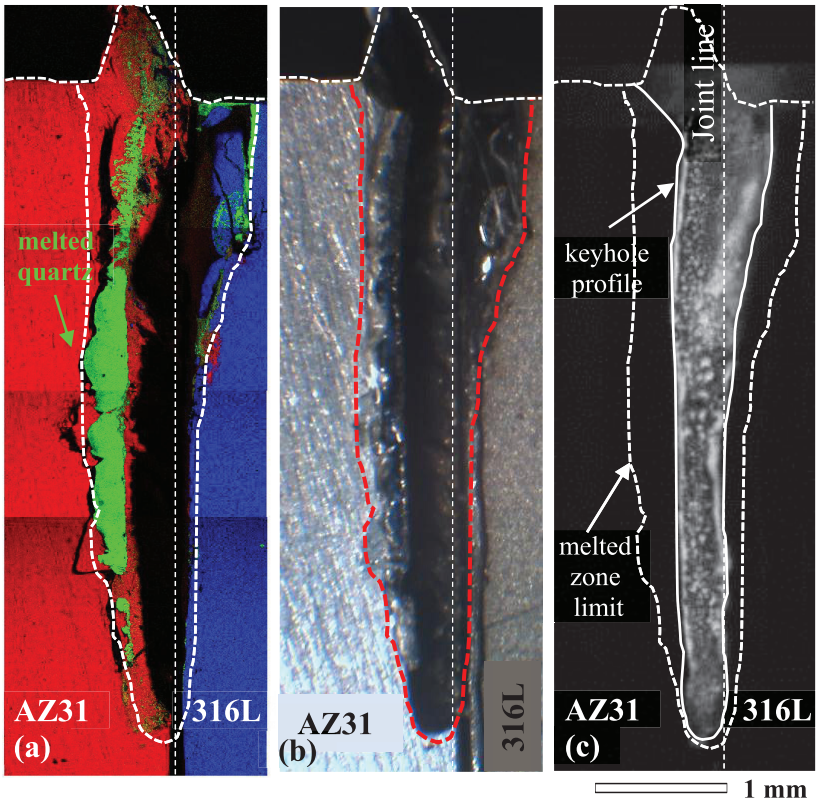

Fig. 6. The AZ31/316L dissimilar couple : X-mapping (a) and optical image (b) of the impact zone compared to the keyhole profile observed at the end of the pulse (c).

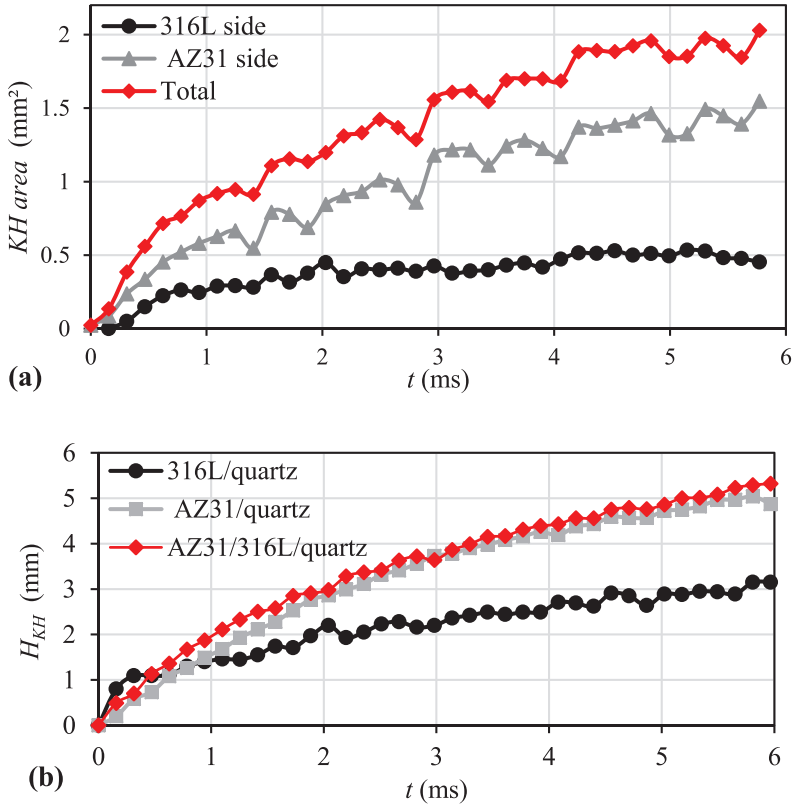

Fig. 7. The evolution of the observable keyhole area in AZ31/316L dissimilar couple (a) and keyhole depth progression during the pulse for the binary metal/quartz and the triple AZ31/316L/quarts combinations (b).

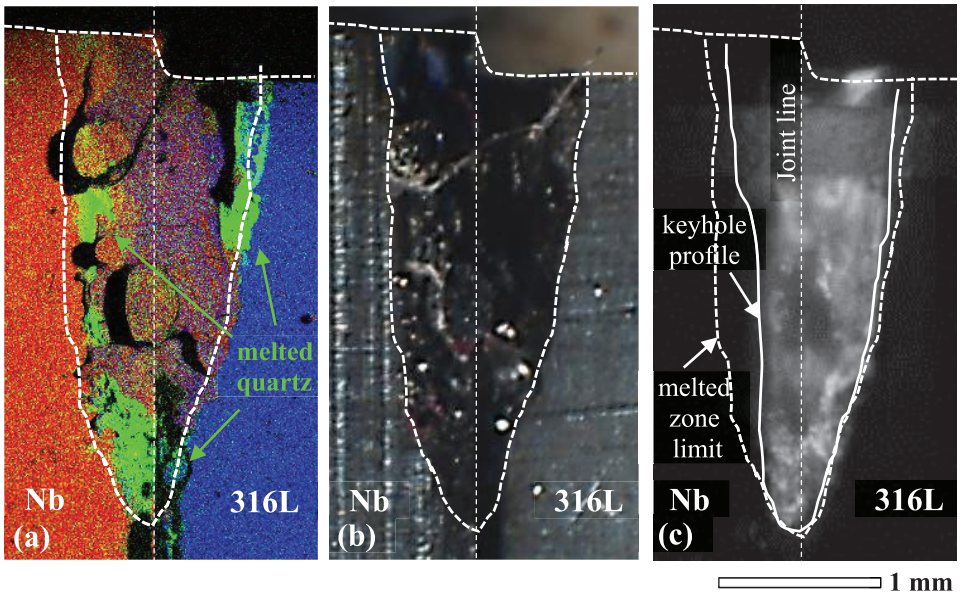

Fig. 8. The niobium/316L dissimilar couple : X-mapping (a) and optical image (b) of the impact zone compared to the keyhole profile observed at the end of the pulse (c).

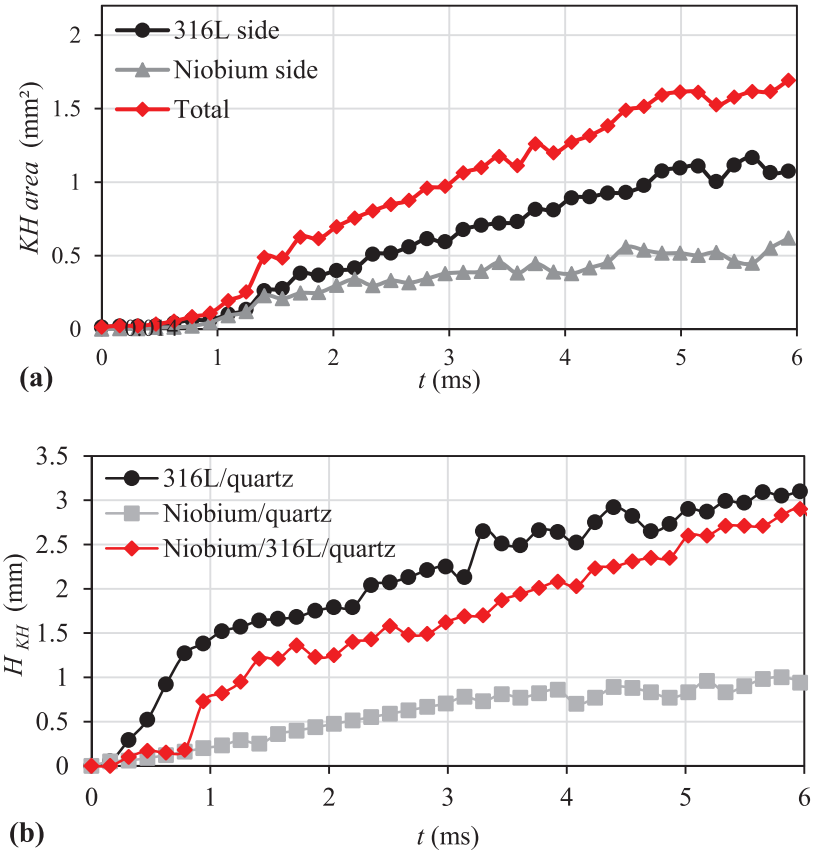

Fig. 9. The evolution of the observable keyhole area in niobium/316L dissimilar couple (a) and keyhole depth progression during the pulse for the binary metal/quartz and the triple niobium/316L/quarts combinations (b).

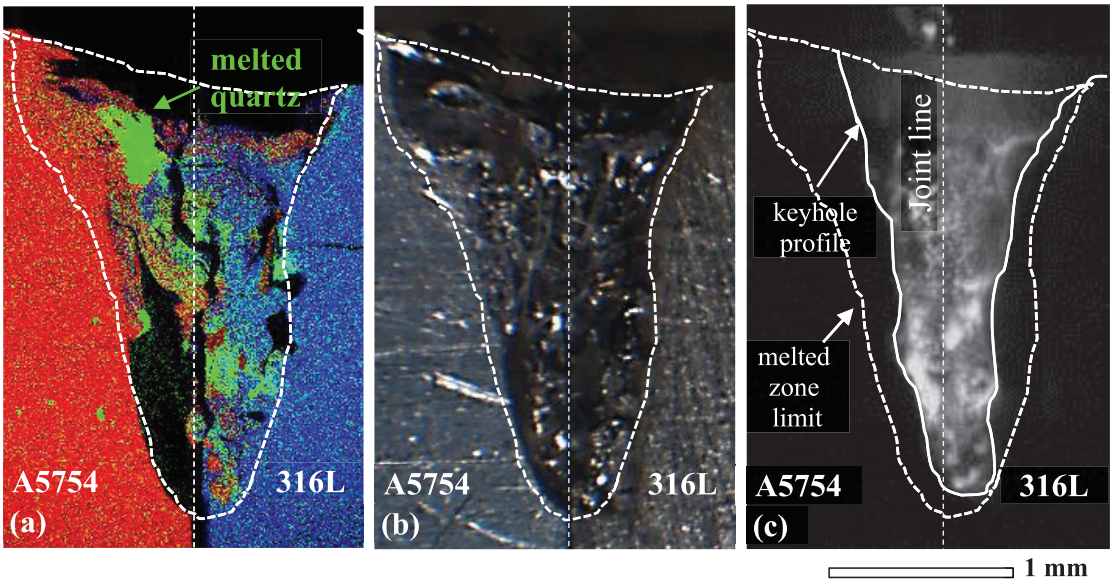

Fig. 10. The A5754/316L dissimilar couple : X-mapping (a) and optical image (b) of the impact zone compared to the keyhole profile observed at the end of the pulse (c).

highly conductive aluminum (Fig. 11b). The A5754/quartz couple showed a long stage of stagnation, with the development of the keyhole only after pulse time > 3 ms. The drilling rate of the keyhole for $t > 1.5$ ms in A5754/316L (0.29 m/s) was intermediate between those of 316L/quartz (0.4 m/s) and AA5754/quartz (0.13 m/s).

The A5754 has a vaporization temperature ~200 K lower than the 316L, however, it only slows down the formation of the keyhole. It can thus be concluded that the mismatch in vaporization temperatures is not the controlling factor in this case, and the keyhole asymmetry is rather influenced by the very high thermal conductivity and the low laser absorption coefficient of the aluminum alloy A5754.

3.6 The copper/316L dissimilar couple

The dissimilar combination copper/316L demonstrated the behavior similar to that of the A5754/316L couple, but the keyhole asymmetry was even more accentuated due to the very high thermal conductivity and the very low absorption coefficient of pure copper to Yb:YAG laser radiation. The melted zone (2190 µm in depth and 1110 µm in width) was still shared between two materials, however, the 316L side was more developed, and the root of the melted zone, as well as the root of the keyhole, were shifted on the 316L side (on the right) by 160 µm (Figs. 12a–12c).

The copper side was involved in the development of the keyhole, due to the synergy with the 316L and sufficiently high energy density, while no keyhole formed in standalone copper/quartz combination. During the first 3 ms of interaction, both metals developed similar keyhole areas (Fig. 13a). Then, the keyhole area on the copper side was slowly increasing up to 0.38 mm^2 or 40%, while on 316L side it expanded more and reached 0.79 mm^2. The final keyhole area of 1.17 mm^2 was significantly lower than that observed in 316L/quartz joint (1.62 ± 0.47 mm^2).

The keyhole depth of the copper/316L joint followed the curve of the 316L/quartz at the beginning of the pulse but progressively slowed down due to the important heat loss through copper (Fig. 13b). The standalone copper did not develop any keyhole. The resulting average drilling rate for the copper/316L combination (0.28 m/s) was about 1.5 times lower to that evaluated for standalone 316L (0.41 m/s).

3.7 The discussion on the factors controlling the keyhole development in the dissimilar joint

The progression of the keyhole during the laser pulse on the metal surface is mainly controlled by:

– the inward heat flux q_{las} that depends on the laser absorption coefficient a and beam parameters such as the power of laser P_l, the radius of laser spot R_l and the time of the pulse t_p:

$$q_{\text{las}} = \frac{2aP_l}{\pi {R_l}^2} \exp^{-2\frac{\left(x^2+y^2\right)}{{R_l}^2}} \left(t \geq t_p\right), \tag{1}$$

– the T-dependent recoil pressure P_{recoil} acting on the surface of the melted zone and conditioned by the vaporization temperature T_{vap} at normal pressure P_0, vaporization energy L_{vap} and the coefficient of vapor recombination β_r [27]:

$$P_{\text{recoil}} = \left(\frac{1+\beta_r}{2}\right) P_0 \exp\left[\frac{L_{\text{vap}} M}{R}\left(\frac{1}{T_{\text{vap}}} - \frac{1}{T}\right)\right], \tag{2}$$

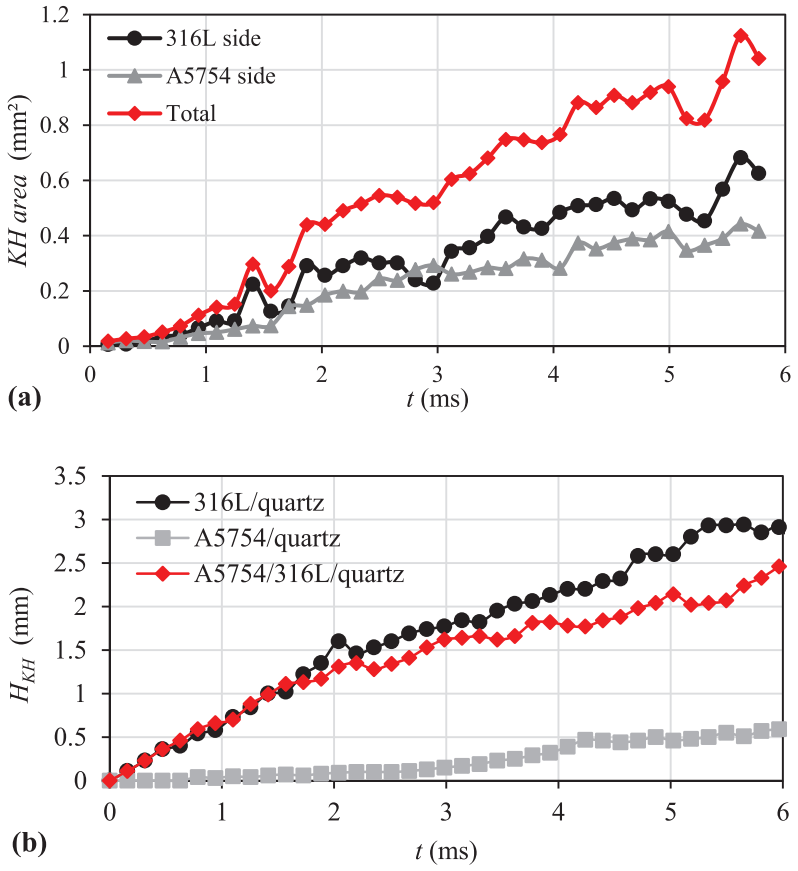

Fig. 11. The evolution of the observable keyhole area in A5754/316L dissimilar couple (a) and keyhole depth progression during the pulse for the binary metal/quartz and the triple A5754/316L/quarts combinations (b).

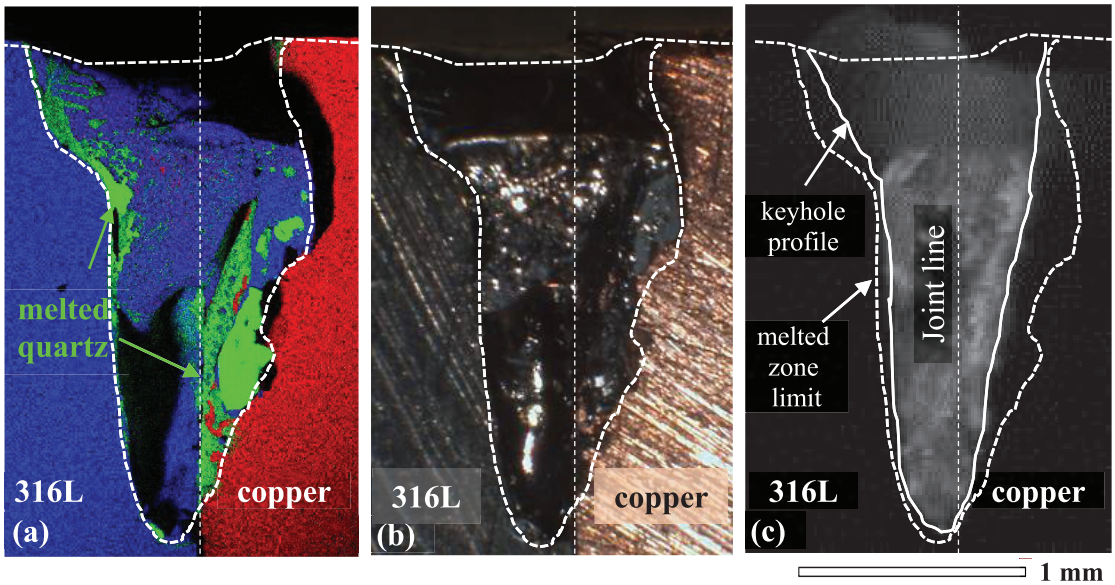

Fig. 12. The copper/316L dissimilar couple: X-mapping (a) and optical image (b) of the impact zone compared to the keyhole profile observed at the end of the pulse (c).

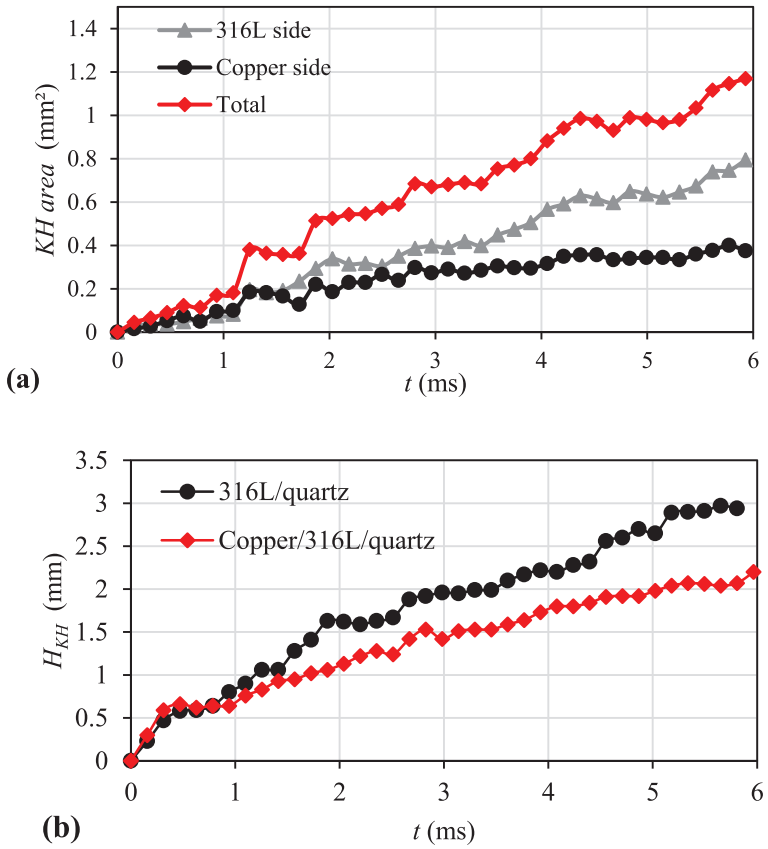

Fig. 13. The evolution of the observable keyhole area in copper/316L dissimilar couple (a) and keyhole depth progression during the pulse for the binary metal/quartz and the triple copper/316L/quartz combinations (b).

– the heat flux of vaporization q_{vap} controlling the drilling rate of the keyhole $\vec{V}_{\text{drill}}$ for the most energetic operational conditions [28]:

$$q_{\text{vap}} = -(1-\beta_r)L_{\text{vap}}\sqrt{\frac{M}{2\pi RT}}P_0 \exp\left[\frac{L_{\text{vap}}M}{R}\left(\frac{1}{T_{\text{vap}}}-\frac{1}{T}\right)\right], \quad (3)$$

$$\overrightarrow{V_{drill}} = \frac{q_{vap}}{\rho}\vec{n}, \quad (4)$$

where M – molar mass, R – ideal gas constant and ρ – density of the metal.

Naturally, the development of the keyhole in case of a dissimilar metal combination is slowed down in the metal that has a low laser absorption coefficient to ~1 μm laser radiation (such as aluminum, copper, gold etc.). Besides the nature of the metal, the local absorption coefficient of laser radiation depends on the used wavelength, but also on the roughness of the unmelted surface and on the surface curvature associated to the formation of the keyhole. In the first place, in order to evaluate the mismatch in properties between different dissimilar combinations, the absorption coefficients to Yb:YAG laser radiation ($\lambda = 1030$ nm) can be estimated for a flat polished surface, that corresponds to the initial stage of laser-metal interaction (a_{ini}). Hagen and Rubens [29] established the relation between T-dependent laser absorption coefficient a_{ini} of polished metallic surface, electric resistivity of the metal δ and radiation wavelength λ in infrared region:

$$a_{\text{ini}} = 0.365\sqrt{\frac{\delta}{\lambda}}, \quad (5)$$

while Wiedemann and Franz [30] described the linear proportionality between the thermal k and electrical σ conductivities of the metal as:

$$k = 2.45 \times 10^{-8} T\sigma. \quad (6)$$

Consequently, the materials with highest thermal conductivity have lowest laser absorption coefficients in the infrared region (Fig. 14a) that can be evaluated for a flat polished surface as:

$$a_{\text{ini}} = 0.365\sqrt{\frac{2.45 \times 10^{-8} T}{\lambda k}}. \quad (7)$$

Since the considered metal combinations have important mismatch in phase change temperatures, for the means of comparison, the absorption coefficients were calculated for the reference temperature of 300 K (Tab. 1).

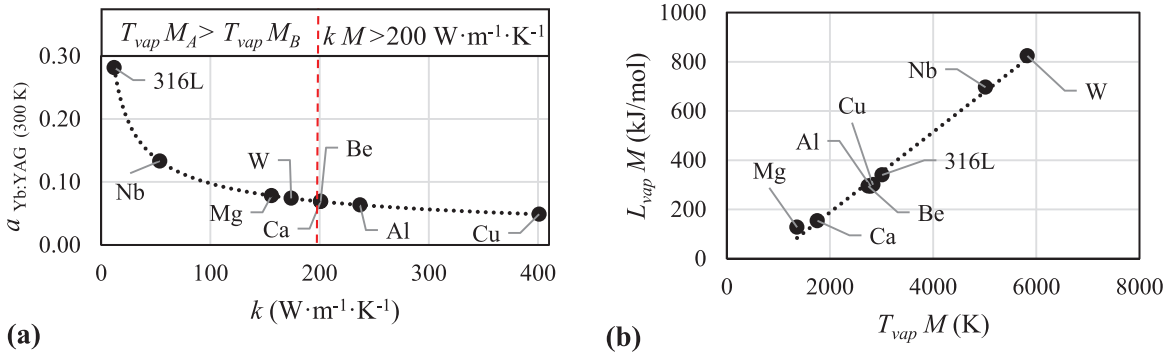

Fig. 14. The illustration of Hagen-Rubens relation (a) and Trouton's rule (b).

With rise of the surface temperature of the melted zone, the absorption coefficients increase, and with the development of the keyhole, further increase is promoted by the phenomenon of multiple reflections. The model of multiple reflections inside the black body developed by Gouffé [31] can be applied to the description of the evolution of absorption coefficient inside the cylindrical keyhole in function of its aspect ratio defined as $\chi = H_{KH}/2R_l$ [32]:

$$a = \frac{a_{ini}}{a_{ini}(2+4\chi)+1-a_{ini}}\left(2+4\chi-\frac{1}{2\chi}(1-a_{ini})\right). \quad (8)$$

This formula can only be applied to a keyhole with aspect ratio $\chi \geq 1$, whereas rather flat melt surface conserves its initial absorption coefficient a_{ini}. As all considered dissimilar combinations (except copper/quartz) satisfy the condition $\chi > 1$, the equation (8) can be used to compare the evolution of absorption coefficients in function of keyhole aspect ratio f the considered dissimilar couples (Fig. 15, Tab. 2). In these calculations, it is admitted that the absorption coefficients of keyhole walls are independent from the nature of the opposite metal and are only defined by the keyhole aspect ratio and a_{ini}. The effect of fused quartz on the diminishing of multiple reflections is not considered in the following discussion and should be studied separately.

For the materials with extremely high thermal conductivity and the resulting low absorption coefficients of Yb:YAG laser radiation, the initiation of the keyhole is inhibited in the same time by the insignificant inward heat flux and by the important conductive heat loss into the solid material, despite their lower vaporization temperature compared to the opposite 316L side. In case of combination with the metal having a rather low thermal conductivity, such as the 316L, the keyhole would tend to shift towards the 316L, and the keyhole formation would be mainly controlled by the inward heat flux, recoil pressure and drilling rate on the 316L side. After the initiation of the keyhole took place, the reflective metal also becomes involved in the keyhole dynamics as its absorption coefficient increases due to the multiple reflections. However, the reflective metal slows down the progression of the keyhole significantly. Such a behavior was observed in the above described A5754/316L (Sect. 3.5) and copper/316L (Sect. 3.6) dissimilar combinations (Tab. 2). For both reflective materials, after creating the keyhole with aspect ratio $\chi = 1$, the absorption coefficient attains ~20%, which is three times lower than for 316L (Figs. 15a and 15b). However, after reaching the final aspect ratio, A5754 side attains the absorption coefficient of 56% ($\chi = 4.5$) and copper only 39% ($\chi = 3.3$), while 316L side remains the most absorbing ($a \sim 85\%$). The slowing down of keyhole progression is reflected by the reduced final aspect ratio of the keyhole in these dissimilar joints compared to the keyhole visible in 316L ($\chi = 4.9$, Sect. 3.1).

Due to the above described keyhole dynamics, the root of the keyholes for these two dissimilar couples is shifted on 316L side. This shift cannot be due to the angle of 3° between the welding head and the verticality, because the welding head is fixed with inclination to the left, while 316L was placed on the right in A5754/316L combination (Fig. 10) and on the left in copper/316L (Fig. 12).

It is also interesting to compare the maximal visible area of the keyhole on 316L side by the end of the pulse in the triple dissimilar joints to a value of half-section found in 316/quartz joints (0.81 mm^2). In case of A5754/316L couple, 316L area reached 0.6 mm^2 or 74% of that of 316/quartz case, while almost identical section was found for copper/316L couple (0.79 mm^2 or 98%). Copper and aluminum has rather close vaporization temperatures, however, aluminum alloys have higher absorption coefficients than copper. In case of A5754/316L couple, the reduction of keyhole area on 316L side compared to 316L/quartz joint can be explained by the evacuation of heat from the interaction zone due to high thermal conductivity of A5754 compared to 316L. On the other hand, in case of copper/316L joint, the particularly high reflectivity of copper brings additional energy to the opposite keyhole wall through the multiple reflections and thus sensibly expands the keyhole volume on 316L side.

In AZ31/316L couple, the better absorbing AZ31 alloy ($a = 32\%$ for $\chi = 1$) produces the keyhole with extremely high final aspect ratio ($\chi = 8.4$), both standalone and in combination with 316L. In these joints, the absorption coefficient of AZ31 reaches (at least theoretically) 100% (Fig. 15c). The deepening of the keyhole compared to standalone 316L is due to the very low vaporization temperature of AZ31, which also contributes to the displacement of keyhole root on AZ31 side. A high keyhole aspect ratio induces the increase of absorption coefficient in 316L side of the keyhole up to 93%. In such a profound keyhole, the absorption coefficients of two materials become very close, despite quite different a_{ini} evaluated for the flat surfaces.

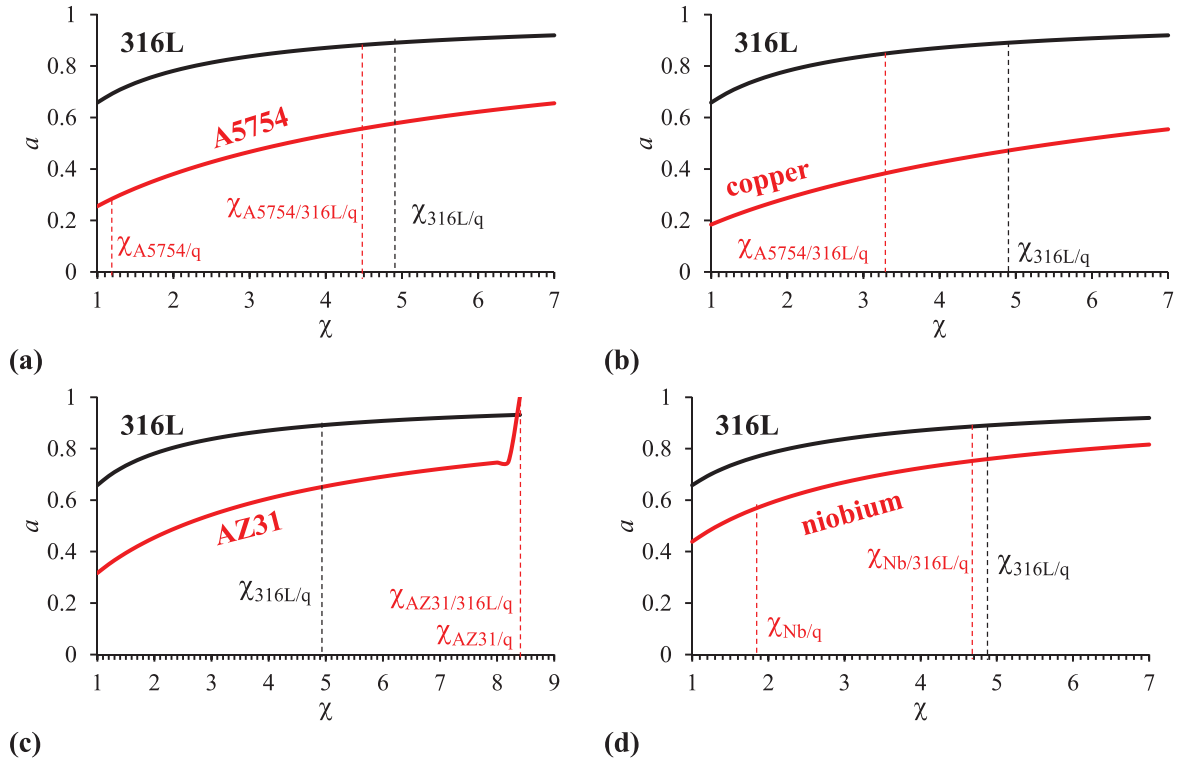

Fig. 15. The evolution of absorption coefficient in function of keyhole ratio for the metals involved in A5754/316L (a), copper/316L (b), AZ31/316L (c) and niobium/316L (d) couples along with indications of maximal keyhole ratio aspects for metal/quartz ($\chi_{M/q}$) and dissimilar/quartz ($\chi_{M1/M2/q}$) combinations.

Table 2. The summary of observed keyhole behaviors.

M/316L joints	AZ31/316L	Nb/316L	A5754/316L	Cu/316L
	T_{vap} M < T_{vap}*316L*	T_{vap} M > T_{vap}*316L*	a M < a *316L*	a M ≪ a *316L*
$\chi^{max}_{M/316L}$	8.4	4.7	4.5	3.3
a^{max}_{M}	1	0.72	0.56	0.39
a^{max}_{316L}	0.93	0.89	0.88	0.85
Root position	Root on AZ31	Centered root	Root on 316L	Root on 316L
Area in metal M	80%	40%	40%	40%
Drilling rate	$V \approx V_{AZ31}$	$V \approx V_{316L}$	$V_{A5754} < V < V_{316L}$	$V \ll V_{316L}$
Controlling factor	T_{vap} M_A> T_{vap} M_B		kM >200 $W \cdot m^{-1} \cdot K^{-1}$	

Niobium exhibits even higher absorption coefficient than AZ31 ($a = 44\%$ for $\chi = 1$), but it slows down the formation of the keyhole because of its much higher vaporization energy compared to 316L. Consequently, the final keyhole aspect ratio is lesser than for 316L ($\chi = 4.7$), and the maximal absorption coefficients expected for niobium and 316L sides of the keyhole are 72 and 89% respectively, which is rather close (Fig. 15d).

In these two couples, the variation of visible area of the keyhole on 316L side also reflects the mismatch in vaporization temperatures. In AZ31/316L dissimilar combination, 316L side of the keyhole reaches only 0.5 mm^2 area, which is 62% of the half-section of the keyhole visible in 316L/quartz joint. This can be explained by the domination of lower-temperature Mg vapor in the keyhole, whereas the keyhole formed in 316L should contain the vapor having a temperature of 3013 K at least (Tab. 1). On the other hand, in niobium/316L dissimilar couple, the keyhole area on 316L side expands to up 1.07 mm^2 or 132% compared to the half-section of the keyhole visible in 316L/quartz joint, which can be explained by the promoting effect of the hotter Nb-rich vapor present in the keyhole.

When the joined metals have the comparable absorption coefficients, the mismatch in their vaporization temperature becomes the main factor of keyhole asymmetry, as it controls in the same time the recoil pressure acting on keyhole walls and the local vaporization rate. According to Trouton's rule [33], the vaporization energy is linearly related to the vaporization temperature (Fig. 14b) due to the close values of the evaporation entropy of substances:

$$L_{\mathrm{vap}} = \Delta S_{\mathrm{vap}} T_{\mathrm{vap}} = (10.5 \mp 0.5) R T_{\mathrm{vap}}. \quad (9)$$

The metals having a lower vaporization temperature (or lower vaporization energy) build up the recoil pressure and vaporization flux before their neighbor, which creates the keyhole shift towards their side. For example, the keyhole formation in AZ31/316L joint (Sect. 3.3) is controlled by AZ31 side, whereas in niobium/316L joint (Sect. 3.4) the 316L side plays the leading role (Tab. 2). Moreover, similar behavior was reproduced numerically for titanium joints with different metals [6] and observed experimentally for the AZ31 in A5754/AZ31 metal combination [3] and for Ti-6Al-4V in the Ti-6Al-4V/niobium combination [2]. In most cases, the keyhole is still shared between the two metals. The exceptions with a complete shift of the keyhole towards a lower T_{vap} material can be found in the study of Grevey et al. [1] on the titanium/tantalum couple and in the study of Torkamany et al. [2] on the Ti6Al4V/niobium couple. On the contrary, the metals with close vaporization temperatures form an almost symmetrical keyhole, such as for the previously described [6] titanium/stainless steel couple.

The question arises, where is the limit between the control of the keyhole asymmetry by the mismatch in *vaporization temperatures (or vaporization energies)* and by the mismatch in *thermal conductivities (or laser absorption coefficients)*? The magnesium alloy AZ31 has thermal conductivity of 156 $\mathrm{W \cdot m^{-1} \cdot K^{-1}}$, which exceeds 10 times the conductivity of 316L, but the keyhole behavior is controlled by the mismatch in vaporization temperatures: it is shifted towards the AZ31. In the same time, aluminum alloy A5754 has a thermal conductivity of 237 $\mathrm{W \cdot m^{-1} \cdot K^{-1}}$, which is ~15 times higher than that of the 316L, and the keyhole behavior in the A5754/316L dissimilar joint is already controlled by the mismatch in thermal conductivity/absorption coefficient. Basing on these observations, one can place the limit between these two mechanisms of keyhole asymmetry around the thermal conductivity of 200 $\mathrm{W \cdot m^{-1} \cdot K^{-1}}$ for the metal joined to the 316L (dash line on the Fig. 14a). The metals which thermal conductivity is intermediate between those of magnesium and aluminum are few: calcium ($k = 200$ $\mathrm{W \cdot m^{-1} \cdot K^{-1}}$), beryllium ($k = 201$ $\mathrm{W \cdot m^{-1} \cdot K^{-1}}$) and tungsten ($k = 174$ $\mathrm{W \cdot m^{-1} \cdot K^{-1}}$). Calcium is not used in a pure form for the engineering purposes due to its low fusion temperature and poor mechanical properties. The vaporization temperature of beryllium ($T_{\mathrm{vap}} = 2744$ K) is close to that of aluminum, and it also has a high thermal conductivity (which corresponds to $a_{\mathrm{ini}} = 0.069$ at 300 K, according to the Eq. (7)). Thus, it is supposed to show the behavior similar to that of aluminum. Tungsten ($T_{\mathrm{vap}} = 5828$ K) has very important mismatch in vaporization temperatures with 316L ($\Delta T_{\mathrm{vap}} > 2800$ K), thus, it can be supposed that for the large set of laser powers the keyhole formation will be dominant on 316L side.

Further work should be dedicated to the numerical modelling of the binary and triple metal/quartz combinations considered in the present discussion. The effect of quartz plate on the heat transfer in the metal(s)/quartz joint should be quantified, in order to develop the possible correction of laser power allowing obtaining the dimensions of the observable interaction zone as close as possible to those obtained by DODO method.

4 Conclusions

- The method of frontal observation of the keyhole through the quartz window was successfully used for imaging of the keyhole in the dissimilar metal combinations between the 316L and different metallic materials. During the pulse, the fused quartz window underwent local melting, however, no keyhole was formed on the quartz side and no cracks were observed. The contact with the fused quartz window produced about 20% increase of the melted zone dimensions in the 316L.
- In the case of the dissimilar combination of 316L with magnesium alloy AZ31 having a lower vaporization temperature, the resulting keyhole was strongly shifted on the AZ31 side. Its visible area and average drilling rate were close to those of AZ31.
- In the case of the dissimilar joint of 316L with pure niobium having a much higher vaporization temperature, the keyhole was more developed on the stainless steel side, and the visible keyhole area as well as the average drilling rate were close to those of 316L/quartz sample.
- In the case of the reflective aluminum alloy A5754 that has a little lower vaporization temperature compared to that of stainless steel, the keyhole was however shifted on the stainless steel side. The visible keyhole area and the average drilling rate were respectively 35% and 25% lower than for 316L/quartz sample.
- In the case of the extremely reflective pure copper having the vaporization temperature little lower to that of stainless steel, the keyhole was strongly shifted on the stainless steel side. The average drilling rate was 50% lower than for 316L/quartz sample, while no keyhole was formed in the standalone copper. Due to the properties of copper, the visible keyhole area was reduced by 28%.
- Basing on the analysis of physical properties of the metals and their interdependencies, it can be concluded that in the case of Yb:YAG laser welding of stainless steel with metals having thermal conductivity ≤ 200 $\mathrm{W \cdot m^{-1} \cdot K^{-1}}$, the keyhole development will be governed by the metal having a lower vaporization temperature. On the other hand, for the 316L combinations with the metals having a thermal conductivity >200 $\mathrm{W \cdot m^{-1} \cdot K^{-1}}$, the keyhole development will remain dominant on the 316L side, but its progression will be slowed down by the influence of the neighboring metal.

Acknowledgements. This research was funded by the Regional Council of Bourgogne Franche-Comté, the Graduate School EIPHI (Contract ANR-17-EURE-0002) and the FEDER. Authors thank Dr. Massaud Mostafa from South Valley University (Qena, Egypt) for providing fused quartz plates.

References

1. D. Grevey, V. Vignal, I. Bendaoud et al., Microstructural and micro-electrochemical study of a tantalum-titanium weld interface, Mater. Des. **87**, 974–985 (2015)
2. M.J. Torkamany, F. Malek Ghaini, R. Poursalehi, An insight to the mechanism of weld penetration in dissimilar pulsed laser welding of niobium and Ti-6Al-4V, Opt. Laser Technol. **79**, 100–107 (2016)
3. I. Tomashchuk, M. Mostafa, T. Caudwell et al., Behavior of laser induced keyhole during dissimilar welding of metals, in: Lasers in Manufacturing Conference 2017, June 26–29, Munich, Germany. https://www.wlt.de/lim/Proceedings2017/Data/PDF/Contribution17_final.pdf
4. Q. Nguyen, A. Azadkhou, M. Akbari et al., Experimental investigation of temperature field and fusion zone microstructure in dissimilar pulsed laser welding of austenitic stainless steel and copper, J. Manufactur. Process. **56**, 206–215 (2020)
5. G. Phanikumar, P. Dutta, K. Chattopadhyay, Continuous welding of Cu-Ni dissimilar couple using CO2 laser, Sci. Technol. Welding Joining **10**, 158–166 (2005)
6. I. Tomashchuk, J.-M. Jouvard, P. Sallamand et al., Modeling of the keyhole asymmetry in dissimilar laser welding, in: Comsol Conference Europe 14–16 October 2020, Virtual Edition. https://www.comsol.fr/paper/modeling-of-the-keyhole-asymmetry-in-dissimilar-laser-welding-94091
7. J.L. Zou, S.K. Wu, W.X. Yang et al., A novel method for observing the micro-morphology of keyhole wall during high-power fiber laser welding, Mater. Des. **80**, 785–790 (2016)
8. A.F.H. Kaplan, R.S. Matti, Absorption peaks depending on topology of the keyhole front and wavelength, J. Laser Appl. **27**, S29012 (2015)
9. H. Kim, K. Nam, S. Oh et al., Deep-learning-based real-time monitoring of full-penetration laser keyhole welding by using the synchronized coaxial observation method, J. Manufact. Process. **68**, 1018–1030 (2021)
10. M. Miyagi, J. Wang, Keyhole dynamics and morphology visualized by in-situ X-ray imaging in laser melting of austenitic stainless steel, J. Mater. Process. Technol. **282**, 116673 (2020)
11. M. Sokolov, P. Franciosa, R. Al Botros et al., Keyhole mapping to enable closed-loop weld penetration depth control for remote laser welding of aluminium components using optical coherence tomography, J. Laser Appl. **32**, 032004 (2019)
12. X. Jin, L. Li, Y. Zhang, A study on Fresnel absorption and reflections in the keyhole in deep penetration laser welding, J. Phys. D: Appl. Phys. **35**, 2304–2310 (2002)
13. X. Jin, P. Berger, T. Graf, Multiple reflections and Fresnel absorption in an actual 3D keyhole during deep penetration laser welding, J. Phys. D: Appl. Phys. **39**, 4703–4712 (2006)
14. Y. Zhang, L. Li, G. Zhang, Spectroscopic measurements of plasma inside the keyhole in deep penetration laser welding, J. Phys. D: Appl. Phys. **38**, 703–710 (2005)
15. M. Zhang, G. Chen, Y. Zhou et al., Direct observation of keyhole characteristics in deep penetration laser welding with a 10 kW fiber laser, Opt. Express **21**, 19997–20004 (2013)
16. Y. Zhang, G. Chen, H. Wei et al., A novel "sandwich" method for observation of the keyhole in deep penetration laser welding, Opt. Lasers Eng. **46**, 133–139 (2008)
17. Y. Arata, H. Maruo, I. Miyamoto et al., Dynamic behavior of laser welding and cutting, in R.A. Bakish (Ed.), Proceedings 7th International Conference on Electron and Ion Beam Science and Technology, Washington, D. C. 1976, pp. 111–128
18. X. Jin, L. Zeng, Y. Cheng, Direct observation of keyhole plasma characteristics in deep penetration laser welding of aluminum alloy 6016, J. Phys. D: Appl. Phys. **45**, 245205 (2012)
19. M. Chen, Y. Wang, G. Yu et al., In situ optical observations of keyhole dynamics during laser drilling, Appl. Phys. Lett. **103**, 194102 (2013)
20. S. Li, G. Chen, M. Zhang et al., Dynamic keyhole profile during high-power deep-penetration laser welding, J. Mater. Process. Technol. **214**, 565–570 (2014)
21. M. Jiang, X. Chen, Y. Chen et al., Increasing keyhole stability of fiber laser welding under reduced ambient pressure, J. Mater. Process. Technol. **268**, 213–222 (2019)
22. A. Artinov, N. Bakir, M. Bachmann et al., Weld pool shape observation in high power laser beam welding, Proc. CIRP **74**, 683–686 (2018)
23. S. Matteï, J.-M. Jouvard, M. Mostafa et al., Comparison of keyhole characteristics obtained by two experimental methods: the "direct observation of drilled hole" method and the "sandwich" method, in: ICALEO 2012-31st International Congress on Applications of Lasers and Electro-Optics, 2012, pp. 59–64
24. J. Schindelin, I. Arganda-Carreras, E. Frise et al., Fiji: an open-source platform for biological-image analysis, Nat. Methods **9**, 676–682 (2012)
25. M. Schneider, L. Berthe, M. Muller et al., A fast method for morphological analysis of laser drilling holes, J. Laser Appl. **22**, 127–131 (2010)
26. S. Guo, J. Zou, J. Xu et al., Multi-stage keyhole evolution in fiber laser welding: an experimental study and theoretical analysis, Res. Phys. **31**, 104943 (2021)
27. R. Fabbro, K. Chouf, Dynamical description of the keyhole in deep penetration laser welding, J. Laser Appl. **12**, 142–148 (2000)
28. C.J. Knight, Theoretical modeling of rapid surface vaporization with back pressure, Am. Inst. Aeronaut. Astronaut. J. **17**, 19–523 (1979)
29. R. Indhu, V. Vivek, L. Sarathkumar et al., Overview of laser absorptivity measurement techniques for material processing, Lasers Manuf. Mater. Process. **5**, 458–481 (2018)
30. G. Wiedemann, R. Franz, Über die Wärme-Leitungsfähigkeit der Metalle, Ann. Phys. Chem. **139**, 497–531 (1853)
31. A. Gouffé, Corrections d'ouverture des corps-noirs artificiels compte tenu des diffusions multiples internes, Rev. Opt. Théorique Instrum. **1-3**, 1–64 (1945)
32. G. Nordet, C. Gorny, Y. Mayi et al., Absorptivity measurements during laser powder bed fusion of pure copper with a 1 kW CW green laser, Opt. Laser Technol. **147**, 107612 (2022)
33. F. Trouton, On molecular latent heat, Philos. Mag. **18**, 54–57 (1884)

Citation de l'article : Iryna Tomashchuk, Mélanie Duband, Jean-Marie Jouvard, In-situ study of keyhole behavior during a laser pulse applied to the dissimilar metal joint, Metall. Res. Technol. **120**, 412 (2023)